Extreme Noise–Extreme El Niño: How State-Dependent Noise Forcing Creates El Niño–La Niña Asymmetry

AARON LEVINE

Department of Atmospheric Sciences, University of Hawai'i at Mānoa, Honolulu, Hawaii, and NOAA/Pacific Marine Environmental Laboratory, Seattle, Washington

FEI FEI JIN

Department of Atmospheric Sciences, University of Hawai'i at Mānoa, Honolulu, Hawaii

MICHAEL J. MCPHADEN

NOAA/Pacific Marine Environmental Laboratory, Seattle, Washington

(Manuscript received 25 January 2016, in final form 22 April 2016)

ABSTRACT

A major open question about El Niño–Southern Oscillation (ENSO) is what causes ENSO amplitude asymmetry, with strong El Niños generally larger than strong La Niñas. The authors examine a leading hypothesis—that the ENSO state modifies the fetch and/or wind speed of westerly wind bursts (WWBs) that create asymmetric forcing and an asymmetric ENSO response. Further, in El Niño forecasts, the number of WWBs expected increases in the month following a strong WWB when compared with the month preceding it. Using a conceptual model, a relationship is derived between the magnitude of the westerly wind burst state dependence on ENSO and ENSO asymmetry. It is found that this relationship between the magnitude of the state dependence and ENSO asymmetry holds in both the observations and 21 coupled climate models. Finally, it is found that because of state-dependent westerly wind burst forcing, extreme El Niño events tend to be of the eastern Pacific variety.

1. Introduction

El Niño–Southern Oscillation (ENSO) has been widely studied as a major phenomenon of the coupled atmosphere–ocean system (Clarke 2008; Sarachick and Cane 2010). Theories that are essentially linear in their dynamics (Suarez and Schopf 1988; Battisti and Hirst 1989; Penland 1996; Penland and Sardeshmukh 1995; Jin 1997) correctly capture the major features of ENSO, the coupling of the atmosphere and ocean and the transition from El Niño to La Niña. However, one of the drawbacks of these theories is their inability to explain certain nonlinear features of ENSO. One of the major unexplained nonlinearities is the ENSO amplitude asymmetry—that the largest El Niño events are generally larger than the largest La Niña events. Understanding what generates this amplitude asymmetry and fuels the largest El Niño events is important because of the large impact that these extreme El Niño events have on society. The largest El Niño on record in 1997/98 is estimated to have cost $34 billion (in 1998 U.S. dollars; Nicholls 2001). To explain the amplitude asymmetry a number of hypotheses have been put forward, including nonlinear dynamic heating (Jin and An 1999; Jin et al. 2003), nonlinear thermocline feedback (DiNezio and Deser 2014), the atmospheric nonlinearity involved in convection (Kang and Kug 2002) or the nonlinearity related to wind stress response to changes in the zonal SST gradient (Liang et al. 2012), biological feedbacks on ENSO (Marzeion et al. 2005), tropical instability waves (Vialard et al. 2001), and multiplicative (i.e., state dependent) noise forcing (Lengaigne

Pacific Marine Environmental Laboratory Contribution Number 4426.

Corresponding author address: Aaron Levine, NOAA/Pacific Marine Environmental Laboratory, 7600 Sand Point Way NE, Seattle 98115, Washington.
E-mail: aaron.levine@noaa.gov

DOI: 10.1175/JCLI-D-16-0091.1

et al. 2004; Eisenman et al. 2005; Gebbie et al. 2007; Chen et al. 2015). Beyond the tropical Pacific, Indian Ocean dynamics have also been explored as a possible source of the amplitude asymmetry (Okumura et al. 2011).

In this paper, we highlight the essential role of the multiplicative noise feedback on ENSO amplitude asymmetry. Early research into ENSO noticed the effect of the short-time-scale weather [westerly wind bursts (WWBs)] on the growth of El Niño events (McPhaden et al. 1988; Yu et al. 2003; Tziperman and Yu 2007). Because the time scale of WWBs is significantly shorter than the time scale of ENSO, they have been incorporated into simple ENSO models as stochastic forcing (Penland 1996; Penland and Sardeshmukh 1995; Moore and Kleeman 1999; Zavala-Garay et al. 2008). Additional research into WWBs suggested that the frequency of WWBs is modulated by the state of ENSO sea surface temperature anomalies (Eisenman et al. 2005). State-dependent noise forcing complements and enhances the low-frequency component of the noise forcing that successfully forces ENSO in a linear system (Roulston and Neelin 2000; Levine and Jin 2010). Thus, state-dependent noise has been incorporated into models ranging from conceptual to coupled GCMs (Eisenman et al. 2005; Gebbie et al. 2007; Chen et al. 2015; Perez et al. 2005; Jin et al. 2007; Gebbie and Tziperman 2009; Kapur and Zhang 2012). When state-dependent noise forcing is included in these models, an increase in El Niño event amplitudes and amplitude asymmetry as well as a change in the location of the maximum El Niño temperature anomalies of El Niño emerges (Lengaigne et al. 2004; Gebbie et al. 2007; Chen et al. 2015; Lopez et al. 2013).

Beyond and related to the ENSO amplitude asymmetry is the ENSO spatial asymmetry. In this case, there appear to be different loci of maximum El Niño variability but only a single locus for La Niña (e.g., Ashok et al. 2007; Takahashi et al. 2011; Ren and Jin 2011). La Niña events are symmetric with the El Niño events that have a similar location of maximum anomaly; however, the strongest El Niño events are centered farther to the east, while there are no similarly eastward-shifted strong La Niña events (Chen et al. 2015). State-dependent noise forcing has been shown to preferentially excite these eastern Pacific El Niño events (Lopez et al. 2013; Lopez and Kirtman 2014; Chen et al. 2015), affecting the spatial and amplitude asymmetry of ENSO.

This paper will elucidate the role of multiplicative noise forcing in creating the El Niño–La Niña asymmetry by tying together evidence from recharge oscillator theory and a conceptual model, reanalysis, and forecast and Coupled Model Intercomparison Project (CMIP) models. We will show that increases in state-dependent noise forcing create more extreme El Niño events by deriving the relationship using the ensemble mean dynamical framework for the recharge oscillator and that this relationship holds throughout the CMIP models. The relationship between state-dependent noise forcing and extreme El Niño events is important for explaining the El Niño–La Niña asymmetries. We will first elaborate on the importance of these WWBs in determining El Niño event magnitude. Using seasonal climate forecasts, we will then show that the number of WWBs increases following a strong WWB when compared with the time preceding the WWB. Then we will explain how state-dependent noise acts to amplify the sum of the noise forcing for the largest El Niño events using a conceptual model. We will also show that the amount of magnification is directly related to the amplitude asymmetry. Finally, we will test this hypothesis in 21 different CMIP5 models using the recently developed method of Levine and Jin (2016) to estimate the magnitude of the state-dependent noise forcing and its corresponding effect on ENSO spatial asymmetry.

2. Data and methods

The results referred to throughout this paper as the reanalysis use the Hadley Centre Sea Ice and Sea Surface Temperature dataset (HadISST; Rayner et al. 2003) and 40-yr ECMWF Re-Analysis (ERA-40) winds (Uppala et al. 2005) and ERA-Interim (Dee et al. 2011) winds when more recent years are examined. The reanalysis is supplemented by 300 years of the 1990 control simulation of the GFDL CM2.1 simulation for comparison (Delworth et al. 2006). The conceptual model used is the same recharge oscillator model as used in Levine and Jin (2016), integrated for 10 000 years for each simulation:

$$\begin{aligned} \frac{dT}{dt} &= -\lambda T + \omega h + \sigma\xi[1 + BH(T)T], \\ \frac{dh}{dt} &= -\omega T, \\ \frac{d\xi}{dt} &= r\xi + w(t). \end{aligned} \tag{1}$$

In this model, λ is a growth rate, ω the natural ENSO frequency, σ the noise amplitude, and ξ is red noise with a 45-day decorrelation time scale r. The coefficients in the model are chosen such that, with $B = 0$, the ENSO amplitude and frequency is approximately the same as observed. El Niño events are defined as a warming that exceeds 0.5 standard deviations for the Niño-3 box (averaged SST anomalies within 90°–150°W and 5°S–5°N), while extreme El Niño events are defined to

have a peak warming exceeding 2.5 standard deviations. Changing the thresholds for events and extreme events results in quantitative but not qualitative changes in the percentage of extreme El Niños that occur; in addition, the relationship of ENSO variability with the state-dependent noise forcing does not fundamentally change.

To calculate the additive noise forcing, we use the method shown in Levine and Jin (2016) to separate the deterministic and stochastic components of the zonal wind stress time series. They systematically remove the effects of the linear and nonlinear Bjerknes feedback (Choi et al. 2013) as well as the combination tones of ENSO with the annual and semiannual cycles from the zonal wind stress (Stuecker et al. 2013), which make up the deterministic component of the wind stress. The residual wind stress is then defined as the stochastic component:

$$\tau_R = \tau - \mu_1 T - \mu_2 H(T) T - \mu_{\mathrm{AC}} T \sin(\omega_A t - t_A) - \mu_{\mathrm{SAC}} T \sin(2\omega_A t - t_s), \quad (2)$$

where τ is the wind stress, T the ENSO state, μ are the coupling coefficients, ω_A is the frequency of the annual cycle, and t_A and t_s are the offsets of the annual and semiannual cycle combination tones, respectively, from the annual cycle in months. We then separate the additive and state-dependent components of the stochastic time series based on their assumptions and results about the characteristics of the state-dependent noise forcing [$\tau_R = \sigma\xi[1 + BH(T)T]$ in Eq. (1), linear dependence on ENSO state BT with a threshold nonlinearity related to convection $H(T)$, all modifying stochastic forcing ξ]. The parameter B is calculated by finding the rate of change of the standard deviation of τ_R as a function of T. Full details of the method can be found in Levine and Jin (2016).

To examine how a WWB alters future forecasts of WWBs, we use the NOAA Climate Forecast System (CFS), version 2. Here we examine two extreme El Niño events, the 1997 event, for which "forecasts" are available through a reforecast experiment (Saha et al. 2014), and the current 2015 event, for which CFS was used operationally. To examine the role of state-dependent noise forcing, we analyze the forecasts generated for the months of May and July 1997 and April and June 2015, examining the change in the WWB predictions following the large WWBs of June 1997 and May 2015. In the reforecast experiment, 9-month forecasts are initialized on the four synoptic hours (0000, 0600, 1200, and 1800 UTC) every 5 days giving us 28 forecasts from May 1997 and 24 forecasts from July. We similarly choose 24 forecasts from April and June 2015. Using the CFS Reanalysis (Saha et al. 2010) and following Levine and Jin (2016), we isolate the total noise forcing from the zonal wind stress. Following Puy et al. (2015), we set the intensity threshold for a WWB at one standard deviation of the wind stress and then choose minimum time duration to be 3 days. The results presented here are not qualitatively dependent on the choice of these thresholds.

TABLE 1. The CMIP5 models and number of years of each simulation used in the calculation. The numbers in the first column refer to the numbers in Fig. 8. (Expansions of acronyms are available online at http://www.ametsoc.org/PubsAcronymList.)

	Model	piControl	RCP4.5	RCP8.5
1	ACCESS1.0	500	95	95
2	ACCESS1.3	500	95	95
3	CanESM2	996	875	380
4	CCSM4	501	674	475
5	CESM1(BGC)	500	95	95
6	CESM1(CAM5)	319	485	285
7	CMCC-CM	330	95	95
8	CMCC-CMS	500	95	95
9	CNRM-CM5	850	295	675
10	CSIRO Mk3.6.0	500	—	95
11	EC-EARTH	452	1140	950
12	FIO-ESM	800	285	95
13	GFDL CM3	800	485	95
14	GFDL-ESM2G	500	95	95
15	GFDL-ESM2M	500	95	95
16	INM-CM4.0	500	95	95
17	IPSL-CM5A-LR	1000	580	580
18	IPSL-CM5A-MR	300	295	—
19	IPSL-CM5B-LR	300	95	95
20	MRI-CGCM3	500	95	95
21	NorESM1-M	501	295	95

The CMIP5 simulations are available from the PCMDI website. The list of the CMIP5 models and lengths of simulation used are listed in Table 1. In the CMIP5 models, to account for the westward El Niño bias, a Niño-3 equivalent box is used. This box is the area-averaged SST anomaly between 5°S and 5°N and 50° longitude long centered on the longitude of largest variance for the tropical Pacific SST first EOF. The skewness is defined as follows: $S = (x' - x)^3[(x' - x)^2]^{-3/2}$. The magnitude of the state-dependent noise forcing for each CMIP5 model is calculated following Levine and Jin (2016) but using the Niño-3 equivalent box defined above; the zonal wind stress is averaged over the box defined by 160°E–160°W and 3°S–3°N, similar to Levine and Jin (2016).

3. Generating an extreme El Niño event

The anomalous heat content of the tropical Pacific Ocean is an important factor in determining the magnitude of an El Niño event (Meinen and McPhaden

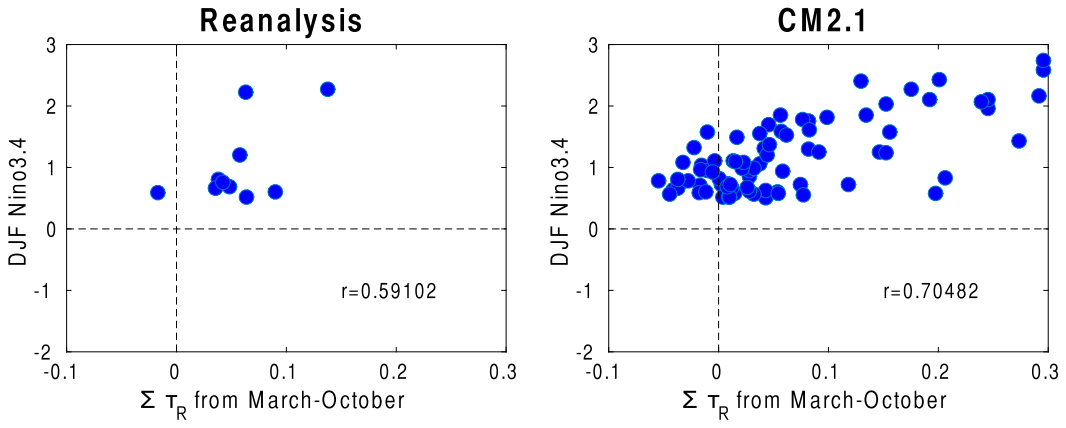

FIG. 1. The relationship of the total noise forcing between March and October to the following DJF Niño-3.4 index for the reanalysis and GFDL CM2.1 for El Niño years.

2000). However, a positive heat content anomaly is not sufficient for producing an El Niño event. The heat content anomaly is better thought of as the energy reservoir that the El Niño event taps into to warm the central and eastern equatorial Pacific. To successfully tap into this reservoir requires additional forcing and the existence of positive feedbacks (Jin et al. 2006). Many previous studies have suggested that this forcing comes from westerly wind events that occur as part of the Bjerknes positive feedback. After removing the deterministic ENSO signal from the zonal wind stress, Levine and Jin (2016) show that the wind stress residual has properties that are mathematically similar to state-dependent noise. Figure 1 shows the dependency of the size of the boreal winter (DJF) SST anomaly in the Niño-3.4 region (5°S–5°N, 170°–120°W) versus the sum of the total nondeterministic (noise) forcing from the previous March through October in the reanalysis and 300 years of the 1990 control simulation from GFDL CM2.1. The stochastic portion of the zonal wind stress during the El Niño growth phase from March to October is clearly an important part of determining the eventual strength of the El Niño event. McPhaden et al. (2006) describe a similar result purely from the observations.

We gain a similar appreciation for the difference in the total noise forcing between the regular and extreme El Niño events by compositing the El Niño events on the peak SST anomaly and comparing the differences in forcing before the peak (Fig. 2). While there are only three extreme El Niño events in the reanalysis dataset, the similarities between the GFDL CM2.1 composite, which composites 15 extreme El Niño events, and the reanalysis composite suggest that the wind stress noise forcing functions similarly in both. Figures 2a–c show how the noise forcing is different for regular and extreme El Niño events. The extreme events have a large sum of noise forcing that is increasing as both the SST anomaly increases and as the peak of the event approaches, whereas the regular El Niño events generally have smaller noise forcing closer to the peak.

However, additive stochastic noise forcing alone cannot explain the ENSO amplitude asymmetry; the alternative hypothesis of state-dependent noise forcing can. Levine and Jin (2016) measured the magnitude and nature of the state dependence of the noise forcing. From their formulation,

$$\xi = \frac{\tau_R}{1 + BH(T)T}, \tag{3}$$

where ξ is the additive component and τ_R is the total noise forcing, we separate the additive and state-dependent $[\xi BH(T)T]$ components of the noise forcing. We examine the fraction of total noise forcing that can be explained by the state-dependent component (Figs. 2d–f) and find that it increases as the El Niño event matures. The state-dependent component is responsible for significantly increasing the noise forcing for the largest El Niño events. This effect is largest when WWBs occur on an already growing El Niño event and expanded western Pacific warm pool (Lopez and Kirtman 2014; Levine et al. 2016, manuscript submitted to *Climate Dyn.*).

Comparing the strong events of 1982/83 and 1997/98 with the recent weak El Niño in the boreal winter of 2014/15 and the growth of a much larger El Niño later in 2015, we can further see the importance of the additional wind stress over time relative to a single triggering westerly wind event (Fig. 3). In February and March 2014, there was a strong westerly wind event that drew comparisons to 1997. Throughout the rest of 1997, there were additional westerly wind events with magnitudes greater than one standard deviation that continued to force El Niño. The resulting El Niño during the boreal winter of 1997/98 is the largest on record. This is compared

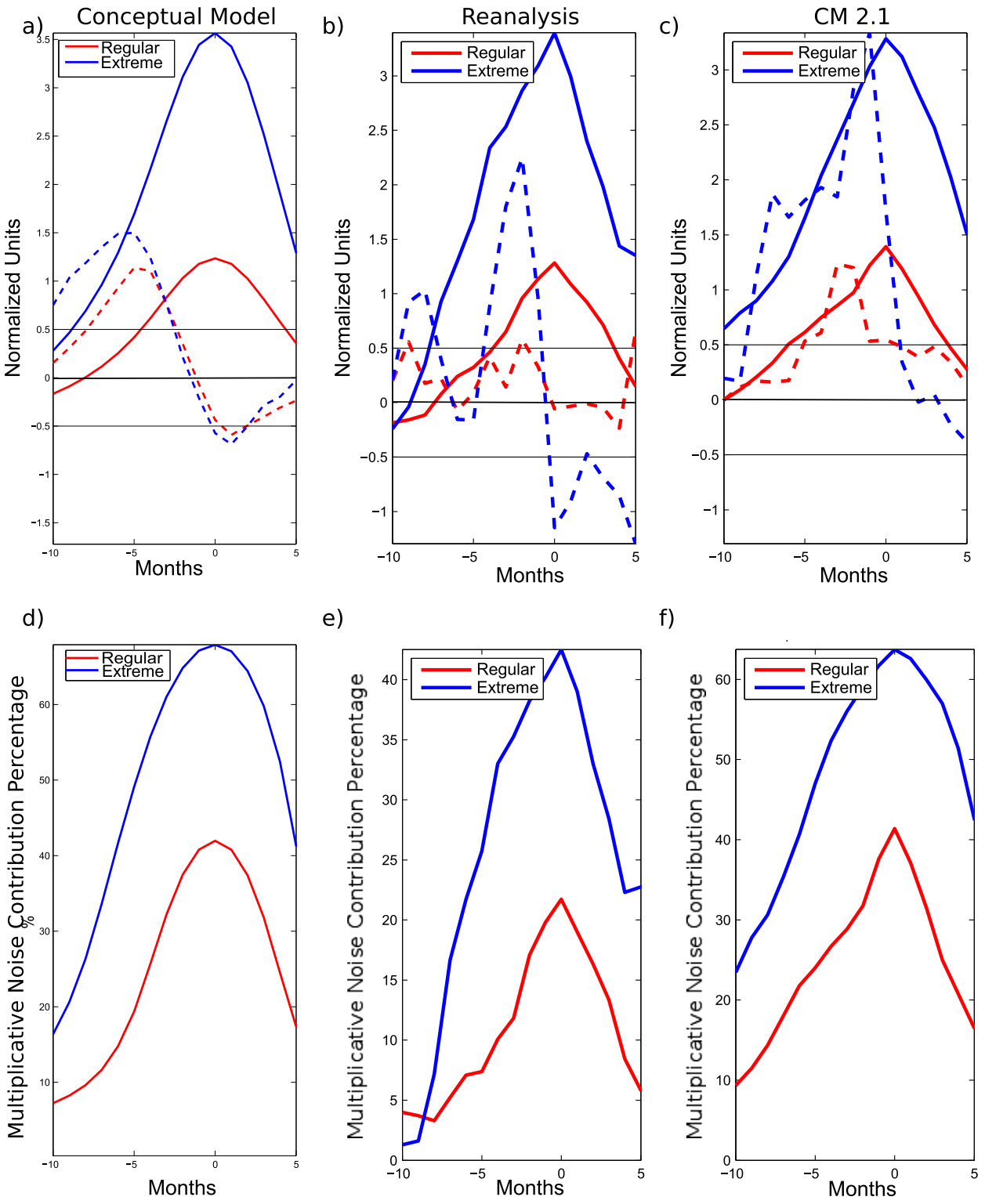

FIG. 2. Multiplicative noise plays a large role in producing extreme El Niño events by significantly increasing the noise forcing during the later portion of the El Niño growth phase, producing a stronger noise forcing as the peak approaches and producing a larger El Niño event. (a)–(c) Composites of El Niño events with temperature (solid) and noise forcing (dashed). (d)–(f) El Niño composites showing the contribution of the state-dependent component of the noise forcing to the total noise forcing.

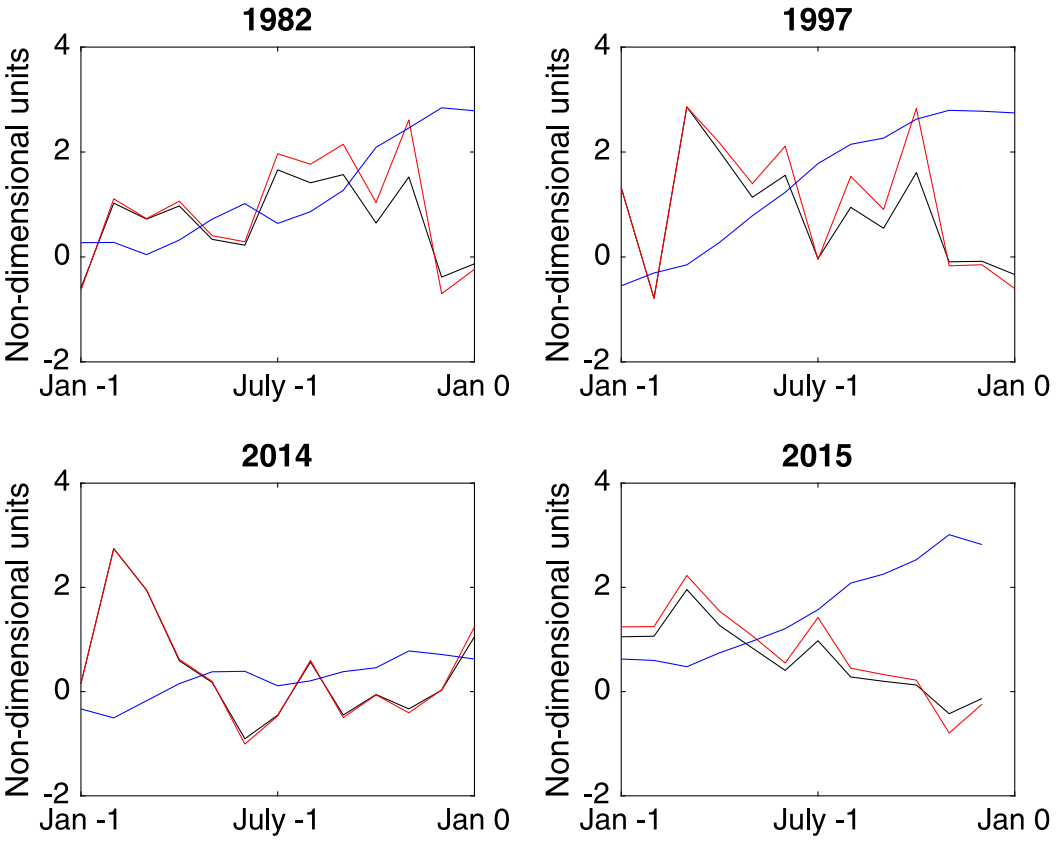

FIG. 3. A comparison of the total noise forcing (red) and additive noise forcing (black) for the 1982/83, 1997/98, 2014/15, and 2015 (through December 2015) El Niño events. ERA-Interim is used here instead of ERA-40 for the wind stress to include the recent years. The Niño-3.4 index is shown by the blue lines. Large initial additive forcing comprises the initial forcing in all cases, but the additional forcing in boreal summer and fall (July–November) exists mostly in 1982 and 1997. In these cases, the additive component no longer accounts for nearly all of the total forcing. State-dependent noise forcing acts to amplify the additive noise forcing for greater total noise forcing in these events.

with what occurred in 2014, where the initial westerly wind event was not followed by any additional strong westerly wind events but in fact an easterly event such that only a very weak El Niño event occurred (Menkes et al. 2014; Hu et al. 2014; McPhaden 2015). The year 2015 follows a very similar pattern to 1997, with multiple strong westerly wind events that continue throughout the boreal spring and summer and state-dependent noise forcing contributing increasingly to the strength of those WWBs as the El Niño event grows in strength. A different example is the 1982/83 event where there were not any large westerly wind events until much later in the year, but the sum of extra westerly wind forcing over the growth phase is large enough to create a large El Niño event.

A key message is that the westerly wind forcing occurs mostly as noise forcing and that the frequency and strength of these WWBs play a large part in the eventual evolution of the El Niño event. State-dependent noise forcing of ENSO implies that as the tropical Pacific cold tongue warms as a result of previous WWBs, the likelihood of an additional WWB increases. To further illustrate this, we count the number of WWBs in each forecast from the initialization time until the beginning of October, normalizing the output into WWBs per month. The results for May and July 1997 and April and June 2015 are shown in Fig. 4. We chose these periods to highlight the changes around the large WWBs of June 1997 and May 2015. As a baseline, using the CFS Reanalysis, which is available for the period from 1979 to 2009, the average number of WWBs per month is 0.5 (Fig. 5). At a 95% confidence level, based on a two-sample Kolmogrov–Smirnov test, the ensemble distributions of WWBs per month for all of the sample months except May 1997 are distinct from the distribution of the 5-month running mean WWBs per month from the reanalysis. Reinforcing that WWBs do not always occur with an anomalously warm tropical Pacific

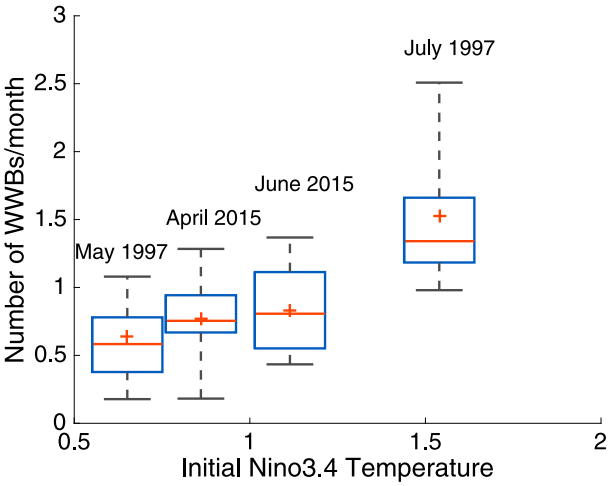

FIG. 4. Box-and-whisker plots of the number of WWBs that occur from the forecasts' initialization through the beginning of October in NOAA CFS prediction models from May and July 1997 and April and June 2015 as a function of initial Niño-3.4 anomaly. The lower and upper limits of the box are the 25th and 75th percentiles, the whiskers extend from the 10th to 90th percentiles, the red line denotes the median, and the red plus denotes the mean value. These distributions show the role that initial temperature and previous WWBs have in increasing the likelihood of additional WWBs as predicted by state-dependent noise.

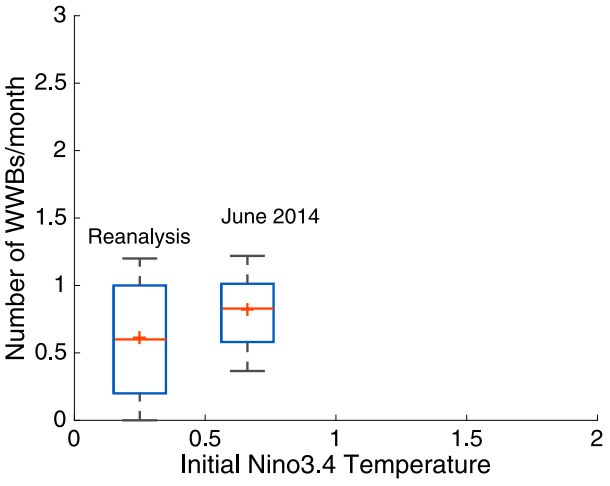

FIG. 5. Box-and-whisker plot in the style of Fig. 4 for the forecasts initialized in June 2014 and for a 5-month running mean of WWBs per month from the reanalysis.

cold tongue, the distribution of predicted WWBs in June 2014 is very similar to May 1997 and April 2015 (Fig. 5). However, unlike in June 1997 and May 2015, in July 2014, an easterly wind burst occurred, and that strongly affected the evolution of El Niño that year toward a weaker event (Menkes et al. 2014; Hu et al. 2014; McPhaden 2015).

In the months preceding the large WWB, both distributions have slightly elevated mean and median WWB frequencies, owing to the already positive Niño-3.4 SST anomalies. In the month after the large WWB, the forecasted number of WWBs per month is larger than the month preceding it. The amount that the mean and median increase is dependent on how much warming occurs in the next month. This is clearly evident from the much larger increase in WWBs per month between May and July 1997, which corresponds with a much larger increase in Niño-3.4 anomalies, than between April and June 2015. Also, the forecasts after the WWBs have greatly increased in the 10th and 25th percentile of WWBs per month when compared with the months preceding the WWB, further reinforcing the increased likelihood of additional WWB events. The 10th percentile of forecasts WWBs per month for June 2015 is approximately the average number of WWBs per month for the reanalysis, while July 1997, in agreement with its much larger initial anomaly, has the 10th percentile of forecasted WWBs per month larger than the average number and the 90th percentile at approximately 5 times the normal rate of WWB occurrence. These results illustrate the significant shift in rate of WWB occurrence as the tropical Pacific warms following WWBs. Our findings with the CFS reforecasts are in agreement with the findings of Vecchi et al. (2006) on the role of stochastic forcing in the 1997/98 El Niño event and strongly implicate the role of state-dependent noise forcing in producing the extreme El Niño event of 1997/98 and the growing extreme El Niño of 2015/16.

4. State-dependent noise forcing and amplitude asymmetry

It has previously been suggested that state-dependent noise forcing can explain ENSO amplitude asymmetry (i.e., that strong El Niño events tend to be larger than strong La Niña events; Lengaigne et al. 2004; Eisenman et al. 2005; Gebbie et al. 2007; Chen et al. 2015). However, the relationship between the state-dependent noise forcing and asymmetry has not yet been demonstrated. Expanding the ensemble mean dynamical framework of Jin et al. (2007) and Levine and Jin (2010) based on the conceptual model in Eq. (1), we derive the dependence of the skewness of ENSO on the magnitude of the state dependence of the noise forcing B (see the appendix):

$$S \propto \frac{2Ba\sqrt{\frac{\sigma^2}{r}}}{\lambda^2 + \frac{1}{2}\omega^2}, \tag{4}$$

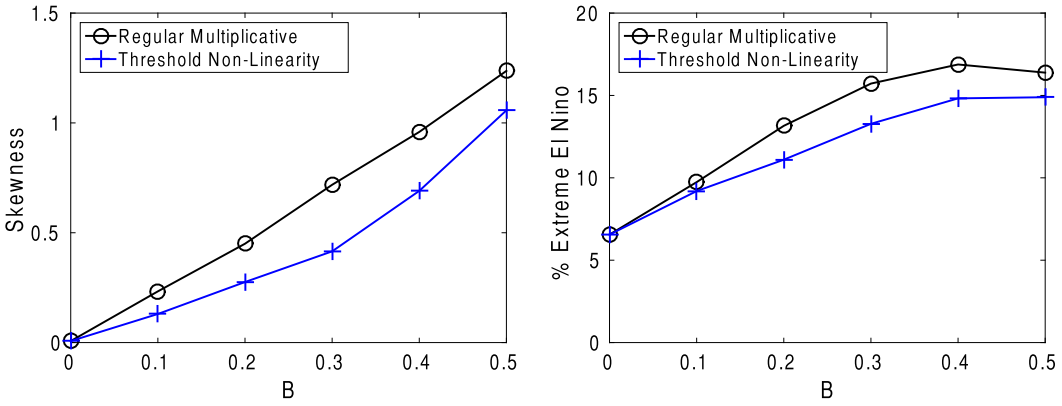

FIG. 6. Using 10 000-yr simulations in the conceptual model, the linear relationship between B and ENSO skewness is clear. It is also clear that the number of extreme El Niño events increases as the value of B increases. The effect of a threshold nonlinearity is also examined resulting from the role of convection in creating state-dependent noise forcing. The threshold nonlinearity has a minor impact on the results.

where a is an empirically derived closure constant. Based on this model, the skewness is linearly dependent on the magnitude of the state-dependence parameter B. It is also proportional to the noise variance σ (how strongly we force the system) and inversely proportional to the growth rate λ (large positive growth rate, the greater the oscillatory dynamics impact size and the system is less skewed; large negative growth rate, the system is more strongly damped and less skewed) and frequency ω (higher frequency, less time to charge the oscillator and less skewed). We can further confirm this by examining long integrations of the conceptual model at different values of the state-dependence parameter B (Fig. 6, left). It is also clear from examining these long integrations that the frequency of the extreme El Niño events as a function of total El Niño events is related to the skewness and the state dependence (Fig. 6, right). Several studies have postulated that this state dependence might be related to the convective nonlinearity (Eisenman et al. 2005; Gebbie et al. 2007; Levine and Jin 2016; Lopez and Kirtman 2014). To account for the minimum SST threshold for convection over the tropical oceans, Levine and Jin (2016) added a threshold nonlinearity to the formulation of state-dependent noise forcing. Figure 6 shows that the effect of this threshold nonlinearity on the amplitude asymmetry is larger for smaller values of the state-dependence parameter B than for larger ones, but both cases still show state-dependent noise forcing as a contributor to skewness.

With this theoretical framework for explaining the ENSO amplitude asymmetry based on state-dependent noise, we apply the method for estimating the state-dependence magnitude from Levine and Jin (2016) to preindustrial control simulations (piControl) and two different emissions scenarios, RCPs 4.5 and 8.5 (RCP4.5 and RCP8.5, respectively), from 21 different CMIP5 models. Figure 7 (left) shows that the models' ENSO skewness falls within the uncertainty (dark gray is one standard deviation, and light gray is two standard deviations) of the value predicted from the conceptual model in Eq. (1) based on the each model's calculated value of B and constant values for all models of λ, ω, and σ. More than half of the models' simulated value of B in preindustrial control simulations is more than one standard deviation from the estimate from reanalysis (Fig. 8 and Table 2). In all but one of these cases, GFDL CM3, the value of B is too low. In examining the global warming simulations, most of the models do not have a consistent trend from the preindustrial control simulation to RCP4.5 to RCP8.5. Three of the models—ACCESS1.0, CESM1(CAM5), and GFDL CM3—show significant increases from preindustrial control to both RCP4.5 and RCP8.5. Of these, only CESM1(CAM5) has a preindustrial control simulation within the estimated range of B from the reanalysis. ACCESS1.0 has too small of a simulated B, and GFDL CM3 has too large of a simulated B. Three models—CCSM4, CNRM-CM5, and IPSL-CM5A-LR—show a consistent significant decrease in B from the preindustrial control simulation to RCP4.5 and RCP8.5. Only two, CCSM4 and CNRM-CM5, of these three models have a reasonable simulation of B in the preindustrial control simulations. IPSC-CM5A-LR has too weak a simulation of B. Overall, it is clear that the CMIP5 models do a poor job in simulating B and have too wide a variance on the change of B due to climate change to draw any strong conclusions as to how these processes will be affected. Our attempts at drawing any strong conclusions about the changes in B due to climate change are also hampered by the uncertainty in estimating B.

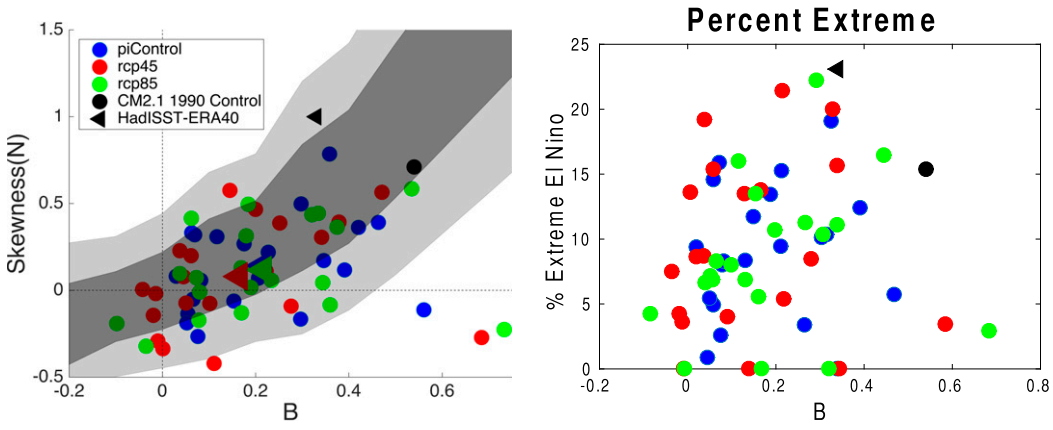

FIG. 7. The CMIP5 models follow the theory for the state-dependent noise forcing vs skewness and extreme events. The multimodel model ensemble shows little difference between the preindustrial control and the RCP4.5 and RCP8.5 emissions scenarios. The reanalysis-calculated values are the black triangles and are also within the uncertainty. The dark gray shading represents one standard deviation around the predicted value of skewness given B, and the light gray shading represents two standard deviations.

In failing to simulate the state dependence correctly, the CMIP models then fail to simulate the observed ENSO skewness. There is not a significant change in the multimodel ensemble values of B or skewness between the control and the different emissions scenarios, in agreement with Zhang and Sun (2014). However, this is most likely a result of the models' inability to correctly simulate the processes associated with state-dependent noise forcing with some half of the models disagreeing on the sign of change from the preindustrial control simulation to the different RCPs.

As expected, B is a good predictor not only of the skewness but also of the percentage of extreme El Niño events (Fig. 7, right). Here again, however, there is not a

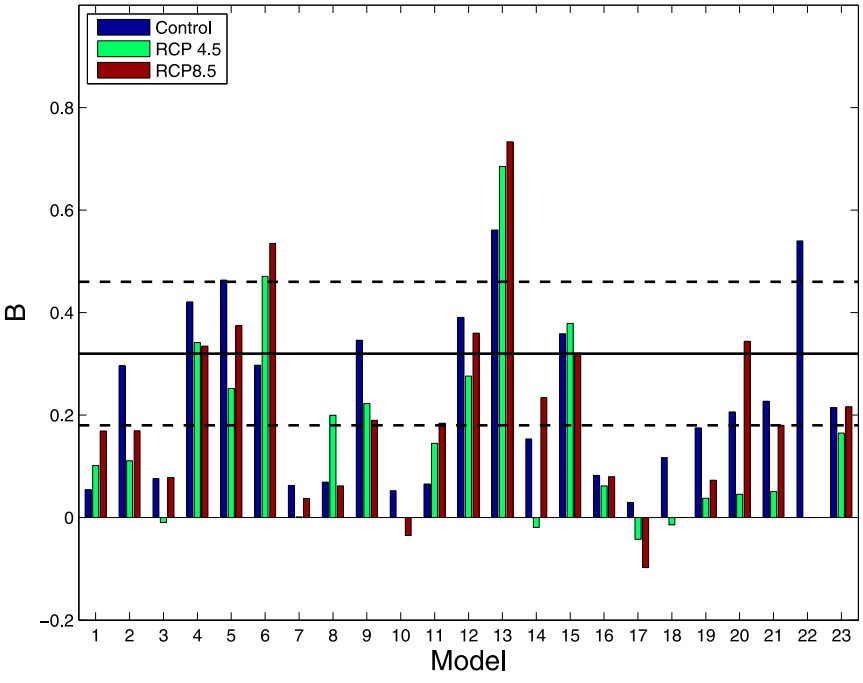

FIG. 8. The state-dependent noise factor for every model examined across the different scenarios used. The GFDL CM2.1 1990 control simulation is 22 and the CMIP5 multimodel ensemble is 23. The solid line is the reanalysis estimate, and the dashed lines represent the one standard deviation values from the reanalysis. Most models fail to simulate multiplicative noise in the preindustrial simulation. Additionally, the models do not agree on the sign change due to climate change.

TABLE 2. The value of B for all models and scenarios used. The uncertainty of the estimation is a function of data length and magnitude of B. From estimates using the conceptual model, for data lengths of approximately 100 years, the uncertainty is approximately ±0.1.

Model	piControl	RCP4.5	RCP8.5
ACCESS1.0	0.05	0.10	0.17
ACCESS1.3	0.30	0.11	0.17
CanESM2	0.08	−0.01	0.08
CCSM4	0.42	0.34	0.33
CESM1(BGC)	0.46	0.25	0.37
CESM1(CAM5)	0.30	0.47	0.53
CMCC-CM	0.06	0.00	0.03
CMCC-CMS	0.07	0.20	0.06
CNRM-CM5	0.35	0.22	0.19
CSIRO Mk3.6.0	0.05	—	−0.03
EC-EARTH	0.07	0.14	0.18
FIO-ESM	0.39	0.28	0.36
GFDL CM3	0.58	0.68	0.73
GFDL-ESM2G	0.15	−0.02	0.23
GFDL-ESM2M	0.36	0.38	0.32
INM-CM4.0	0.08	0.06	0.08
IPSL-CM5A-LR	0.03	−0.04	−0.10
IPSL-CM5A-MR	0.12	−0.01	—
IPSL-CM5B-LR	0.18	0.04	0.07
MRI-CGCM3	0.21	0.05	0.34
NorESM1-M	0.23	0.05	0.18

significant difference between the different emissions scenarios and the preindustrial control simulation. This result is different from the finding of Cai et al. (2014), who found an increase in the extreme El Niño events due to global warming. However, we are using an index based on normalized sea surface temperature anomalies, whereas they defined extremes based on a precipitation index in the Niño-3 region. Our result is similar to other studies of ENSO and climate change that use temperature-based indices (Zhang and Sun 2014; Bellenger et al. 2014).

5. State-dependent noise forcing and spatial asymmetry

Compositing the extreme El Niño events in the CMIP5 models shows that the models that have larger values of B have larger extreme events with the location of maximum SST anomaly shifted eastward when compared with those models that have smaller values of B (Fig. 9). This eastward shift of the location of maximum SST anomaly is closer to the reanalysis extreme El Niño composite, although still failing to capture the bulk of the warming between the South American coast and the cold tongue that is present in the reanalysis. Additionally, while still simulating an El Niño that extends too far to the west, the extent of the western Pacific El Niño bias is reduced in these models that have a larger value of B.

Previous analyses of extreme El Niño events suggest that they are all eastern Pacific (EP)-type El Niños in contrast to central Pacific (CP)-type El Niños (Takahashi and Dewitte 2015). Previous research has also shown that state-dependent noise forcing disproportionately affects EP El Niño events (Lopez and Kirtman 2014). Given the CMIP5 models' poor ability to capture state-dependent noise forcing and extreme El Niño events, it is unsurprising that they do not capture the spatial pattern of ENSO skewness well (Zhang and Sun 2014; Bellenger et al. 2014). In general, the models have a bullseye of skewness in the central Pacific cold tongue region and a region of enhanced skewness along the coast, but these two regions have a region of zero or negative skewness in between them (Fig. 10).

While the multimodel ensemble skewness fails to capture the correct spatial pattern, the better an individual model's ability to generate multiplicative noise, the more positive (negative) the SST asymmetry is in the eastern (western) tropical Pacific (Fig. 11). This is a manifestation of the interaction between noise forcing and El Niño type. El Niño events cluster into two (Takahashi and Dewitte 2015) or three (Chen et al. 2015) types. The transition between different groups happens as the size of the El Niño event increases. The warm pool advection that occurs following a WWB produces an increased likelihood of larger following WWBs (Puy et al. 2015; Levine et al. 2016, manuscript submitted to *Climate Dyn.*). If additional WWBs do not occur, the warm pool returns to its climatological values. The zonal advection of warm pool temperatures into the central Pacific can produce a central Pacific El Niño event. However, if the additional noise forcing does occur, the magnitude of the forcing is likely to be greater because of the state-dependent component of the noise forcing. Since El Niño event magnitude is directly related to the total noise forcing, this additional forcing makes it more likely to cross over the thresholds that separate the extreme El Niño events from the normal El Niño events.

6. Summary and discussion

Here we have presented a theoretical explanation for how state-dependent noise forcing can account for ENSO amplitude asymmetry and the creation of extreme El Niño events. The theory has been tested in a linear, damped, noise-forced recharge oscillator model. Reanalyses and 21 CMIP5 models have been evaluated and found to fit with the theoretical expectations for ENSO amplitude asymmetry and frequency of extreme events. Unfortunately, because of the CMIP5 models' inability to correctly simulate the state-dependent noise forcing, we are not able to come to a conclusion about

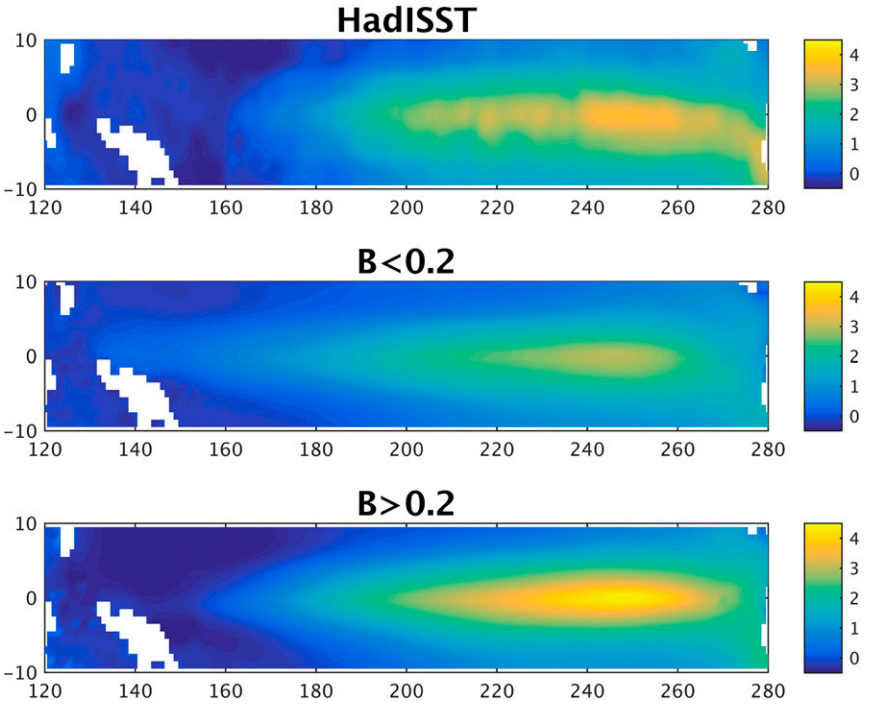

FIG. 9. Composites of extreme El Niño events for the (top) reanalysis and CMIP multimodel ensemble (MME) for (middle) $B < 0.2$ and (bottom) $B > 0.2$. The models with the larger values of B have strong extreme El Niño events that have the location of maximum SST anomaly more consistent with the reanalysis.

the potential changes to extreme El Niño events in terms of SST anomalies due to global warming (Bellenger et al. 2014).

We find that the CMIP5 models that best simulate state-dependent noise do a better job of simulating the broad spectrum of El Niño events, and in particular, in the models with better state-dependent noise, the extreme El Niño events occur farther to the east and are more asymmetric than those models that fail to simulate state-dependent noise forcing, in agreement with the single-model studies of Lopez and Kirtman (2014), Chen et al. (2015), and Takahashi and Dewitte (2015). The relationship between these two nonlinearities, state-dependent noise forcing and spatial asymmetry, in the ENSO system is related to the changing of relative importance of the different feedbacks throughout the equatorial Pacific. In the central Pacific, the zonal advection feedback dominates, while in the eastern Pacific the thermocline feedback dominates (Chen et al. 2015). State-dependent noise encapsulates the response of convection to the advection of the western Pacific warm pool (Puy et al. 2015; Levine et al. 2016, manuscript submitted to *Climate Dyn.*). Since B measures how strongly the SST–wind–precipitation feedback responds to the initial wind stress noise, we expect that the tropical mean state biases impact these results. In agreement with Zhang and Sun (2014), we find that model simulation of B, and therefore ENSO asymmetry, is strongly correlated with the equatorial cold tongue bias (Fig. 12). As the convection shifts and any WWBs that occur become stronger, the thermocline feedback in the eastern Pacific is more strongly forced. As this feedback kicks in, the eastern Pacific El Niño grows and can cross the extreme event threshold (Takahashi and Dewitte 2015), physically linking the state-dependent noise nonlinearity to the spatial asymmetry. Models that have an overly strong equatorial cold tongue do not shift convection far enough east often enough to trigger this response regularly.

Reinforcing the idea that it is the low-frequency component of the noise forcing that is important for forcing ENSO (Roulston and Neelin 2000; Levine and Jin 2010), the sum of the total noise forcing is more important for determining the eventual size of the El Niño event than the exact timing of the WWBs as long as they continue to occur throughout the growth phase of El Niño. There are large differences in the timing of the WWBs between the 1982/83, 1997/98, and 2015/16 events, but all three have substantial WWB forcing over the preceding March–October, which largely explains the size of the two extreme El Niño events and the predicted size of the 2015/16 event.

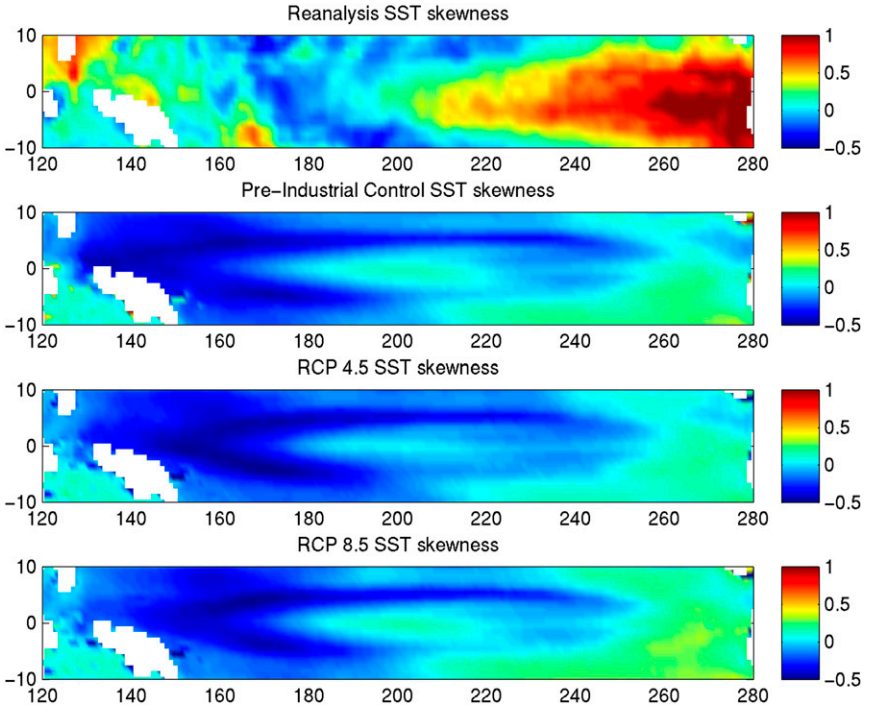

FIG. 10. The skewness of the SST anomaly for (top)–(bottom) reanalysis and CMIP MME for preindustrial control, RCP4.5, and RCP8.5. None of the MMEs correctly capture SST anomaly asymmetry in the equatorial regions.

Given that the amplitude asymmetry of ENSO can be well explained by state dependence of noise forcing, we infer that extreme El Niño events depend not only on high ocean heat content (Meinen and McPhaden 2000) but also on the excitation from WWBs (Chen et al. 2015). A single WWB is not enough, but in a state-dependent system a single WWB makes additional WWBs more likely to occur. This was seen in the experiment by Lengaigne et al. (2004), who inserted a WWB into their coupled model in 10 ensemble members, leading to an increase in the number of El Niño and extreme El Niño events that occurred in the experimental ensemble compared with the control ensemble. They also found that only when the initial WWB was followed by additional WWBs did the model simulate extreme El Niños.

A consequence to the finding of the role of state-dependent noise of the amplitude asymmetry of ENSO is that the upper limit of the potential predictability of the extreme El Niño events is reduced. State-dependent noise forcing of ENSO has already been shown to increase the forecast spread (Levine and Jin 2010; Vecchi et al. 2006; Lopez and Kirtman 2014; Levine and McPhaden 2015). In particular, using the same conceptual model, Levine and Jin (2010) found that the growth rate of the second moment was $\mathrm{GR} \approx -\lambda + 2a\sigma^2 B^2/r$, increasing the ensemble spread quadratically in response to any biases in B. However, it is also worth noting that there is a large spread between reanalysis products and within model simulations of both λ and σ, which means that model-simulated potential predictability could be correct, dependent on the cancellation of errors from different sources. This quantification also ignores the seasonal cycle of ENSO growth rate (Stein et al. 2010; Dommenget and Yu 2016). The seasonal cycle of

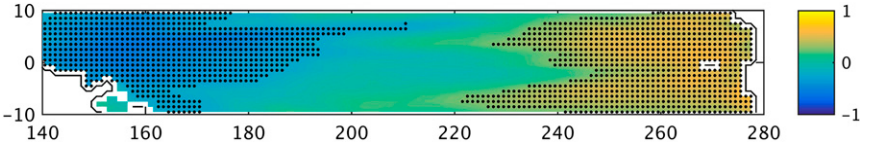

FIG. 11. Spatial correlation of the CMIP5 models' value of B with the SST skewness in the tropical Pacific. Regions of statistical significance are stippled.

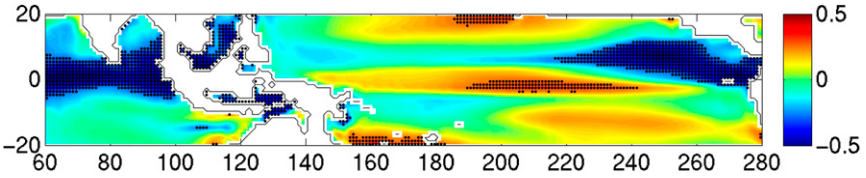

FIG. 12. Spatial correlation of the CMIP5 models' value of B with the SST difference from the model's tropical mean SST. Regions of statistical significance are stippled. Models that simulate the equatorial cold tongue better more accurately simulate B.

ENSO growth rate contributes to the spring predictability barrier and is more prominent when state-dependent noise is included (Levine and McPhaden 2015), also considering that a seasonally dependent growth rate means the timing of the wind stress noise forcing is also important (Levine and McPhaden 2016). Attempts to further quantify the interactions between state-dependent noise forcing and the seasonal cycle of ENSO growth rate are ongoing. Since the largest El Niños are more noise driven than previously assumed and individual weather events are unpredictable on seasonal time scales, then extreme El Niño events are likely to have a larger spread of potential sea surface temperature anomalies. An example of this enhanced uncertainty can be seen by comparing the spring and summer of 2014 to the spring and summer of 1997 and 2015. In 2014, an easterly wind burst occurred, which helped to shut down the development of an El Niño event after large WWBs in January–March 2014 led some in the El Niño forecasting community to believe that an extreme El Niño was going to occur (Menkes et al. 2014; Hu et al. 2014; McPhaden 2015). In contrast, with similar Niño-3.4 SST anomalies prevailing, WWBs occurred in the boreal spring and summer of 1997 and 2015, which aided in forcing the extreme El Niño events the following winters. These results emphasize that, in addition to improvements in computer models, assimilation techniques, and observing systems, research to enhance the utility of seasonal forecasts should focus on probabilistic as opposed to deterministic approaches, particularly during the early stages of developing ENSO events.

Acknowledgments. The authors thank A. Kumar and W. Wang for providing the 2015 CFS forecasts and two anonymous reviewers for their helpful feedback. AFZL and JFF were supported by NSF Grant AGS-1034798, U.S. Department of Energy Grant DE-SC0005110, and NOAA Grant NA10OAR4310200. Part of this research was performed while AFZL held a National Research Council Research Associateship Award at NOAA/PMEL. MJM is supported by NOAA. The reanalysis products are available online for HadISST (http://www.metoffice.gov.uk/hadobs/hadisst/) and for ERA-40 and ERA-Interim (http://apps.ecmwf.int/datasets). The CFS Reanalysis, reforecasts, and current forecast archive are available online as well (http://nomads.ncdc.noaa.gov/data.php?name=access#cfs). The 2015 forecasts should be available shortly. The CMIP5 data are available through the PCMDI archive (http://cmip-pcmdi.llnl.gov/cmip5/data_portal.html).

APPENDIX

Derivation of the Dependence of Skewness on B

Starting from the second- and third-order terms in Levine and Jin (2010), we can add additional equations to solve analytically for the skewness, $S = T'^3(T'^2)^{-3/2}$:

$$\frac{d\langle T'^2\rangle}{dt} = -2\lambda\langle T'^2\rangle + 2\omega\langle h'T'\rangle + 2\sigma(1 + B\langle T\rangle)\langle \xi T'\rangle + 2\sigma B\langle \xi T'^2\rangle,$$

$$\frac{d\langle h'^2\rangle}{dt} = -2\omega\langle h'T'\rangle,$$

$$\frac{d\langle h'T'\rangle}{dt} = -\lambda\langle h'T'\rangle + \omega(\langle h'^2\rangle - \langle T'^2\rangle) + \sigma(1 + B\langle T\rangle)\langle \xi h'\rangle + 2\sigma B\langle \xi h'T'\rangle, \quad \text{(A1)}$$

where angle brackets refer to the ensemble mean. By multiplying $(1/3)Td\langle T'^2\rangle/dt$ the equation for the third-moment evolution of the temperature is found:

$$\frac{d\langle T'^3\rangle}{dt} = -6\lambda\langle T'^3\rangle + 6\omega\langle h'T'^2\rangle + 6\sigma(1+B\langle T\rangle)\langle \xi T'^2\rangle + 6\sigma B\langle \xi T'^3\rangle. \quad \text{(A2)}$$

Similarly, by multiplying $(1/3)hd\langle h'^2\rangle/dt$ the equation for the third-moment evolution heat content is found:

$$\frac{d\langle h'^3\rangle}{dt} = -2\omega\langle h'^2T'\rangle. \quad \text{(A3)}$$

Finally, the mixed term $d\langle h'T'^2\rangle/dt$ is solved for by multiplying $hd\langle T'^2\rangle/dt + (1/2)Td\langle h'T'\rangle/dt$:

$$\frac{d\langle h'T'^2\rangle}{dt} = -2\lambda\langle h'T'^2\rangle + 2\omega\langle h'^2T'\rangle + 2\sigma(1+B\langle T\rangle)\langle \xi h'T'\rangle - 2\lambda\langle h'T'^2\rangle + 2\sigma(1+B\langle T\rangle)\langle \xi h'T'\rangle + 2\omega(\langle h'^2T'\rangle - \langle T'^3\rangle) + 4\sigma B\langle \xi h'T'^2\rangle, \quad \text{(A4)}$$

which simplifies to the following:

$$\frac{d\langle h'T'^2\rangle}{dt} = -4\lambda\langle h'T'^2\rangle - 2\omega\langle T'^3\rangle + 4\omega\langle h'^2T'\rangle + 4\sigma(1+B\langle T\rangle)\langle \xi h'T'\rangle + 4\sigma B\langle \xi h'T'^2\rangle. \quad \text{(A5)}$$

By assuming steady state, $d/dt = 0$, so from Eq. (A3),

$$\langle h'^2T'\rangle = 0. \quad \text{(A6)}$$

Substituting into Eq. (A5) and assuming fourth-order closure condition, $\langle \xi h'T'^2\rangle = 0$, and $\langle \xi h'T'\rangle = 0$:

$$0 = -4\lambda\langle h'T'^2\rangle - 2\omega\langle T'^3\rangle \quad \text{and} \quad \text{(A7)}$$

$$\langle h'T'^2\rangle = \frac{-\omega}{2\lambda}\langle T'^3\rangle. \quad \text{(A8)}$$

Substituting into Eq. (A2),

$$0 = -6\lambda\langle T'^3\rangle - 6\omega\frac{\omega}{2\lambda}\langle T'^3\rangle + 6\sigma B\langle \xi T'^3\rangle + 6\sigma B\langle \xi T'^2\rangle, \quad \text{(A9)}$$

which yields the following:

$$\langle T'^3\rangle = \frac{\sigma B\langle \xi T'^3\rangle + \sigma\langle \xi T'^2\rangle}{\lambda^2 + \frac{1}{2}\omega^2}. \quad \text{(A10)}$$

Returning to Levine and Jin (2010), we find that

$$\frac{d\langle \xi T'^2\rangle}{dt} = -(2\lambda + r)\langle \xi T'^2\rangle + 2\omega\langle \xi h'T'\rangle + 2\sigma(1+B\langle T\rangle)\langle \xi^2T'\rangle - 2\sigma B(\xi^2T'^2 - \langle \xi T'\rangle^2). \quad \text{(A11)}$$

Again assuming steady state, $r \gg \lambda$, and closure conditions $\langle \xi h'T'\rangle = 0$, $\langle \xi T'\rangle^2 = 0$, and $\langle \xi^2T'^2\rangle = 2a\langle T'^2\rangle$,

$$0 = -r\langle \xi T'^2\rangle + 2\sigma\langle \xi^2T'\rangle - 4\sigma Ba\langle T'^2\rangle, \quad \text{(A12)}$$

which yields

$$\langle \xi T'^2\rangle = \frac{2\sigma}{r}(\langle \xi^2T'\rangle - 2Ba\langle T'^2\rangle). \quad \text{(A13)}$$

From Levine and Jin (2010),

$$\frac{d\langle \xi^2T'\rangle}{dt} = -(\lambda + 2r)\langle \xi^2T'\rangle + \omega\langle \xi^2h'\rangle + \sigma B\langle \xi^3T'\rangle. \quad \text{(A14)}$$

Again assuming steady state, $r \gg \lambda$, and that closure conditions $\langle \xi^2h'\rangle = 0$ and $\langle \xi^3T'\rangle = 2a\langle \xi T'\rangle$,

$$0 = -2r\langle \xi^2T'\rangle + \sigma 2Ba\langle \xi T'\rangle, \quad \text{(A15)}$$

which yields

$$\langle \xi^2T'\rangle = \frac{\sigma}{r}Ba\langle \xi T'\rangle. \quad \text{(A16)}$$

From Levine and Jin (2010),

$$\frac{d\langle \xi T'\rangle}{dt} = -(\lambda + r)\langle \xi T'\rangle + \omega\langle \xi h'\rangle + \sigma(1+B\langle T\rangle) + \sigma B\langle \xi^2T'\rangle. \quad \text{(A17)}$$

Again assuming steady state, $r \gg \lambda$, and that closure conditions $\langle \xi h'\rangle = 0$ and $\langle \xi^2T'\rangle = 0$,

$$0 = -r\langle \xi T'\rangle + \sigma, \quad \text{(A18)}$$

which yields

$$\langle \xi T'\rangle = \frac{\sigma}{r}. \quad \text{(A19)}$$

Plugging Eq. (A19) into Eq. (A16),

$$\langle \xi^2T'\rangle = \frac{\sigma^2}{r^2}Ba. \quad \text{(A20)}$$

Plugging Eq. (A20) into Eq. (A13),

$$\langle \xi T'^2 \rangle = \frac{2\sigma}{r} Ba \left(\frac{\sigma^2}{r^2} - 2\langle T'^2 \rangle \right). \quad \text{(A21)}$$

Assuming the fourth-order closure condition $\langle \xi T'^3 \rangle = 2a \langle \xi T' \rangle \langle T'^2 \rangle$ and plugging into Eq. (A10),

$$\langle T'^3 \rangle = \frac{\frac{-4Ba\sigma^2}{r} \langle T'^2 \rangle + \frac{2Ba\sigma^3}{r^3}}{\lambda^2 + \frac{1}{2}\omega^2}. \quad \text{(A22)}$$

Since $r^3 \gg r$,

$$\frac{\langle T'^3 \rangle}{\langle T'^2 \rangle} = \frac{\frac{2Ba\sigma^2}{r}}{\lambda^2 + \frac{1}{2}\omega^2}. \quad \text{(A23)}$$

Skewness is defined as $T'^3 (T'^2)^{-3/2}$, so we must also solve for T'^2. Assuming steady state in Eq. (A1) and $\langle h' T' \rangle = 0$ yields

$$0 = -2\lambda \langle T'^2 \rangle + 2\sigma \langle \xi T' \rangle + 2\sigma B \langle \xi T'^2 \rangle. \quad \text{(A24)}$$

Substituting in Eqs. (A21) and (A19) and solving for $\langle T'^2 \rangle$ yields

$$\langle T'^2 \rangle = \frac{\frac{\sigma^2}{r} \left(1 + 2B^2 a \frac{\sigma^2}{r} \right)}{\lambda + 4B^2 a \frac{\sigma^2}{r}}. \quad \text{(A25)}$$

Taking the square root of Eq. (A25) and $r^2 \gg r$,

$$\sqrt{\langle T'^2 \rangle} = \sqrt{\frac{\frac{\sigma^2}{r}}{\lambda + 4B^2 a \frac{\sigma^2}{r}}}. \quad \text{(A26)}$$

Since

$$\frac{\langle T'^3 \rangle}{\langle T'^2 \rangle} \frac{1}{\sqrt{\langle T'^2 \rangle}} = \frac{\langle T'^3 \rangle}{(\langle T'^2 \rangle)^{3/2}},$$

divide Eq. (A23) by Eq. (A26):

$$S = \frac{\langle T'^3 \rangle}{(\langle T'^2 \rangle)^{3/2}} = \frac{2Ba\sqrt{\frac{\sigma^2}{r}}}{\lambda^2 + \frac{1}{2}\omega^2} \sqrt{\lambda + 4B^2 a \frac{\sigma^2}{r}}. \quad \text{(A27)}$$

And thus the skewness is linearly dependent on B.

REFERENCES

Ashok, K., S. K. Behera, S. A. Rao, H. Weng, and T. Yamagata, 2007: El Niño Modoki and its possible teleconnection. *J. Geophys. Res.*, **112**, C11007, doi:10.1029/2006JC003798.

Battisti, D. S., and A. C. Hirst, 1989: Interannual variability in a tropical atmosphere–ocean model: Influence of the basic state, ocean geometry and nonlinearity. *J. Atmos. Sci.*, **46**, 1687–1712, doi:10.1175/1520-0469(1989)046<1687:IVIATA>2.0.CO;2.

Bellenger, H., E. Guilyardi, J. Leloup, M. Lengaigne, and J. Vialard, 2014: ENSO representation in climate models: From CMIP3 to CMIP5. *Climate Dyn.*, **42**, 1999–2018, doi:10.1007/s00382-013-1783-z.

Cai, W., and Coauthors, 2014: Increasing frequency of extreme El Niño events due to greenhouse warming. *Nat. Climate Change*, **4**, 111–116, doi:10.1038/nclimate2100.

Chen, D., and Coauthors, 2015: Strong influence of westerly wind bursts on El Niño diversity. *Nat. Geosci.*, **8**, 339–345, doi:10.1038/ngeo2399.

Choi, K., G. A. Vecchi, and A. Wittenberg, 2013: ENSO transition, duration, and amplitude asymmetries: Role of the nonlinear wind stress coupling in a conceptual model. *J. Climate*, **26**, 9462–9476, doi:10.1175/JCLI-D-13-00045.1.

Clarke, A. J., 2008: *An Introduction to the Dynamics of El Niño and the Southern Oscillation*. Academic Press, 324 pp.

Dee, D., and Coauthors, 2011: The ERA-Interim reanalysis: Configuration and performance of the data assimilation system. *Quart. J. Roy. Meteor. Soc.*, **137**, 553–597, doi:10.1002/qj.828.

Delworth, T. L., and Coauthors, 2006: GFDL's CM2 global coupled climate models. Part I: Formulation and simulation characteristics. *J. Climate*, **19**, 643–674, doi:10.1175/JCLI3629.1.

DiNezio, P. N., and C. Deser, 2014: Nonlinear controls on the persistence of La Niña. *J. Climate*, **27**, 7335–7355, doi:10.1175/JCLI-D-14-00033.1.

Dommenget, D., and Y. Yu, 2016: The seasonally changing cloud feedbacks contribution to the ENSO seasonal phase-locking. *Climate Dyn.*, doi:10.1007/s00382-016-3034-6, in press.

Eisenman, I., L. Yu, and E. Tziperman, 2005: Westerly wind bursts: ENSO's tail rather than the dog? *J. Climate*, **18**, 5224–5238, doi:10.1175/JCLI3588.1.

Gebbie, G., and E. Tziperman, 2009: Predictability of SST-modulated westerly wind bursts. *J. Climate*, **22**, 3894–3909, doi:10.1175/2009JCLI2516.1.

——, I. Eisenman, A. Wittenberg, and E. Tziperman, 2007: Modulation of westerly wind bursts by sea surface temperature: A semistochastic feedback of ENSO. *J. Atmos. Sci.*, **64**, 3281–3295, doi:10.1175/JAS4029.1.

Hu, S., A. V. Fedorov, M. Lengaigne, and E. Guilyardi, 2014: The impact of westerly wind bursts on the diversity and predictability of El Niño events: An ocean energetics perspective. *Geophys. Res. Lett.*, **41**, 4654–4663, doi:10.1002/2014GL059573.

Jin, F.-F., 1997: An equatorial ocean recharge paradigm for ENSO. Part I: Conceptual model. *J. Atmos. Sci.*, **54**, 811–829, doi:10.1175/1520-0469(1997)054<0811:AEORPF>2.0.CO;2.

——, and S.-I. An, 1999: Thermocline and zonal advective feedbacks within the equatorial ocean recharge oscillator model for ENSO. *Geophys. Res. Lett.*, **26**, 2989–2992, doi:10.1029/1999GL002297.

——, ——, A. Timmermann, and J. Zhao, 2003: Strong El Niño events and nonlinear dynamical heating. *Geophys. Res. Lett.*, **30**, 1120, doi:10.1029/2002GL016356.

——, L. L. Pan, and M. Watanabe, 2006: Dynamics of synoptic eddy and low-frequency flow feedback. Part I: A dynamic closure. *J. Atmos. Sci.*, **63**, 1677–1694, doi:10.1175/JAS3715.1.

——, L. Lin, A. Timmermann, and J. Zhao, 2007: Ensemble-mean dynamics of the ENSO recharge oscillator under state-dependent stochastic forcing. *Geophys. Res. Lett.*, **34**, L03807, doi:10.1029/2006GL027372.

Kang, I.-S., and J.-S. Kug, 2002: El Niño and La Niña sea surface temperature anomalies: Asymmetry characteristics associated with their wind stress anomalies. *J. Geophys. Res.*, **107**, 4372, doi:10.1029/2001JD000393.

Kapur, A., and C. Zhang, 2012: Multiplicative MJO forcing of ENSO. *J. Climate*, **25**, 8132–8147, doi:10.1175/JCLI-D-11-00609.1.

Lengaigne, M., E. Guilyardi, J. P. Boulanger, C. Menkes, P. Delecluse, P. Inness, J. Cole, and J. Slingo, 2004: Triggering El Niño by westerly wind events in a coupled general circulation model. *Climate Dyn.*, **23**, 601–620, doi:10.1007/s00382-004-0457-2.

Levine, A. F. Z., and F. F. Jin, 2010: Noise-induced instability in the ENSO recharge oscillator. *J. Atmos. Sci.*, **67**, 529–542, doi:10.1175/2009JAS3213.1.

——, and ——, 2016: A simple approach to quantifying noise–ENSO interaction. Part I: Deducing the state-dependency of the windstress forcing using monthly data. *Climate Dyn.*, doi:10.1007/s00382-015-2748-1, in press.

——, and M. J. McPhaden, 2015: The annual cycle in ENSO growth rate as a cause of the spring predictability barrier. *Geophys. Res. Lett.*, **42**, 5034–5041, doi:10.1002/2015GL064309.

——, and ——, 2016: How the July 2014 easterly wind burst gave the 2015–2016 El Niño a head start. *Geophys. Res. Lett.*, doi:10.1002/2016GL069204, in press.

Liang, J., X.-Q. Yang, and D.-Z. Sun, 2012: The effect of ENSO events on the tropical Pacific mean climate: Insights from an analytical model. *J. Climate*, **25**, 7590–7606, doi:10.1175/JCLI-D-11-00490.1.

Lopez, H., and B. P. Kirtman, 2014: WWBs, ENSO predictability, the spring barrier and extreme events. *J. Geophys. Res. Atmos.*, **119**, 10 114–10 138, doi:10.1002/2014JD021908.

——, ——, E. Tziperman, and G. Gebbie, 2013: Impact of interactive westerly wind bursts on CCSM3. *Dyn. Atmos. Oceans*, **59**, 24–51, doi:10.1016/j.dynatmoce.2012.11.001.

Marzeion, B., A. Timmermann, R. Murtugudde, and F.-F. Jin, 2005: Biophysical feedbacks in the tropical Pacific. *J. Climate*, **18**, 58–70, doi:10.1175/JCLI3261.1.

McPhaden, M. J., 2015: Playing hide and seek with El Niño. *Nat. Climate Change*, **5**, 791–795, doi:10.1038/nclimate2775.

——, H. P. Freitag, S. P. Hayes, B. A. Taft, Z. Chen, and K. Wyrtki, 1988: The response of the equatorial Pacific Ocean to a westerly wind burst in May 1986. *J. Geophys. Res.*, **93**, 10 589–10 603, doi:10.1029/JC093iC09p10589.

——, X. Zhang, H. H. Hendon, and M. C. Wheeler, 2006: Large scale dynamics and MJO forcing of ENSO variability. *Geophys. Res. Lett.*, **33**, L16702, doi:10.1029/2006GL026786.

Meinen, C. S., and M. J. McPhaden, 2000: Observations of warm water volume changes in the equatorial Pacific and their relationship to El Niño and La Niña. *J. Climate*, **13**, 3551–3559, doi:10.1175/1520-0442(2000)013<3551:OOWWVC>2.0.CO;2.

Menkes, C. E., M. Lengaigne, J. Vialard, M. Puy, P. Marchesiello, S. Cravatte, and G. Cambon, 2014: About the role of westerly wind events in the possible development of an El Niño in 2014. *Geophys. Res. Lett.*, **41**, 6476–6483, doi:10.1002/2014GL061186.

Moore, A. M., and R. Kleeman, 1999: Stochastic forcing of ENSO by the intraseasonal oscillation. *J. Climate*, **12**, 1199–1220, doi:10.1175/1520-0442(1999)012<1199:SFOEBT>2.0.CO;2.

Nicholls, N., 2001: Atmospheric and climatic hazards: Improved monitoring and prediction for disaster mitigation. *Nat. Hazards*, **23**, 137–155, doi:10.1023/A:1011130223164.

Okumura, Y. M., M. Ohba, C. Deser, and H. Ueda, 2011: A proposed mechanism for the asymmetric duration of El Niño and La Niña. *J. Climate*, **24**, 3822–3829, doi:10.1175/2011JCLI3999.1.

Penland, C., 1996: A stochastic model of IndoPacific sea surface temperature anomalies. *Physica D*, **98**, 534–558, doi:10.1016/0167-2789(96)00124-8.

——, and P. D. Sardeshmukh, 1995: The optimal growth of tropical sea surface temperature anomalies. *J. Climate*, **8**, 1999–2024, doi:10.1175/1520-0442(1995)008<1999:TOGOTS>2.0.CO;2.

Perez, C. L., A. M. Moore, J. Zavala-Garay, and R. Kleeman, 2005: A comparison of the influence of additive and multiplicative stochastic forcing on a coupled model of ENSO. *J. Climate*, **18**, 5066–5085, doi:10.1175/JCLI3596.1.

Puy, M., J. Vialard, M. Lengaigne, and E. Guilyardi, 2015: Modulation of equatorial Pacific westerly/easterly wind events by the Madden–Julian oscillation and convectively-coupled Rossby waves. *Climate Dyn.*, **46**, 2155–2178, doi:10.1007/s00382-015-2695-x.

Rayner, N. A., D. E. Parker, E. B. Horton, C. K. Folland, L. Alexandre, D. P. Rowell, E. C. Kent, and A. Kaplan, 2003: Global analyses of sea surface temperature, sea ice, and night marine air temperature since the late nineteenth century. *J. Geophys. Res.*, **108**, 4407, doi:10.1029/2002JD002670.

Ren, H.-L., and F.-F. Jin, 2011: Niño indices for two types of ENSO. *Geophys. Res. Lett.*, **38**, L04704, doi:10.1029/2010GL046031.

Roulston, M. S., and J. D. Neelin, 2000: The response of an ENSO model to climate noise, weather noise and intraseasonal forcing. *Geophys. Res. Lett.*, **27**, 3723–3726, doi:10.1029/2000GL011941.

Saha, S., and Coauthors, 2010: The NCEP Climate Forecast System Reanalysis. *Bull. Amer. Meteor. Soc.*, **91**, 1015–1057, doi:10.1175/2010BAMS3001.1.

——, and Coauthors, 2014: The NCEP Climate Forecast System version 2. *J. Climate*, **27**, 2185–2208, doi:10.1175/JCLI-D-12-00823.1.

Sarachick, E., and M. Cane, 2010: *The El Niño-Southern Oscillation Phenomenon*. Cambridge University Press, 369 pp.

Stein, K., N. Schneider, A. Timmermann, and F.-F. Jin, 2010: Seasonal synchronization of ENSO events in a linear stochastic model. *J. Climate*, **23**, 5629–5643, doi:10.1175/2010JCLI3292.1.

Stuecker, M. F., A. Timmermann, F. F. Jin, S. McGregor, and H. Ren, 2013: A combination mode of the annual cycle and the El Niño/Southern Oscillation. *Nat. Geosci.*, **6**, 540–544, doi:10.1038/ngeo1826.

Suarez, M. J., and P. S. Schopf, 1988: A delayed action oscillator for ENSO. *J. Atmos. Sci.*, **45**, 3283–3287, doi:10.1175/1520-0469(1988)045<3283:ADAOFE>2.0.CO;2.

Takahashi, K., and B. Dewitte, 2015: Strong and moderate nonlinear El Niño regimes. *Climate Dyn.*, **46**, 1627–1645, doi:10.1007/s00382-015-2665-3.

——, A. Montecinos, K. Goubanova, and B. Dewitte, 2011: ENSO regimes: Reinterpreting the canonical and Modoki El Niño. *Geophys. Res. Lett.*, **38**, L10704, doi:10.1029/2011GL047364.

Tziperman, E., and L. Yu, 2007: Quantifying the dependence of westerly wind bursts on the large-scale tropical Pacific SST. *J. Climate*, **20**, 2760–2768, doi:10.1175/JCLI4138a.1.

Uppala, S. M., and Coauthors, 2005: The ERA-40 reanalysis. *Quart. J. Roy. Meteor. Soc.*, **131**, 2961–3012, doi:10.1256/qj.04.176.

Vecchi, G., A. Wittenberg, and A. Rosati, 2006: Reassessing the role of stochastic forcing in the 1997–1998 El Niño. *Geophys. Res. Lett.*, **33**, L01706, doi:10.1029/2005GL024738.

Vialard, J., C. Menkes, J. P. Boulanger, P. Delecluse, E. Guilyardi, M. J. McPhaden, and G. Madec, 2001: A model study of

oceanic mechanisms affecting equatorial Pacific sea surface temperature during the 1997–98 El Niño. *J. Phys. Oceanogr.*, **31**, 1649–1675, doi:10.1175/1520-0485(2001)031<1649:AMSOOM>2.0.CO;2.

Yu, L., R. A. Weller, and T. W. Liu, 2003: Case analysis of a role of ENSO in regulating the generation of westerly wind bursts in the western equatorial Pacific. *J. Geophys. Res.*, **108**, 3128, doi:10.1029/2002JC001498.

Zavala-Garay, J., C. Zhang, A. M. Moore, A. Wittenberg, M. J. Harrison, A. Rosati, J. Vialard, and R. Kleeman, 2008: Sensitivity of hybrid ENSO models to unresolved atmospheric variability. *J. Climate*, **21**, 3704–3721, doi:10.1175/2007JCLI1188.1.

Zhang, T., and D.-Z. Sun, 2014: ENSO asymmetry in CMIP5 models. *J. Climate*, **27**, 4070–4093, doi:10.1175/JCLI-D-13-00454.1.